energies

MDPI

Article

Virtual Synchronous Machine Testing and System Split Resilience: A Comparative Analysis with Grid-Following PV Inverters

Ibrahim Okikiola Lawal [1,*], Horst Schulte [1,*] and Ammar Salman [2]

[1] Control Engineering Group, Department of Engineering, HTW Berlin-University of Applied Sciences, 13353 Berlin, Germany
[2] Fraunhofer Institute for Solar Energy Systems (Fraunhofer ISE), 79110 Freiburg im Breisgau, Germany; ammar.salman@ise.fraunhofer.de
* Correspondence: ibrahim.o.lawal@ntnu.no (I.O.L.); schulte@htw-berlin.de (H.S.)

Abstract

The increasing penetration of converter-interfaced generation raises critical concerns for power system stability, especially during rapid transients and system split events that are not yet adequately addressed in current grid code compliance tests. This paper assesses the resilience of a Virtual Synchronous Machine (VSM) in comparison with a grid-following photovoltaic (PV) inverter through a combined framework of standardized benchmark tests and realistic system split scenarios. In benchmark testing, the VSM provided synthetic inertia by delivering a transient-power burst from a 0.30 p.u. setpoint to 0.545 p.u. (on a 20 MVA base, representing 54.5% of rated capacity) under a −0.4 Hz/s frequency ramp, corresponding to an equivalent inertia constant of approximately 15 s. With the limited frequency-sensitive mode–underfrequency (LFSM-U) function enabled, it sustained additional active power up to 0.61 p.u. once the frequency fell below 49.8 Hz. The PV inverter, by contrast, demonstrated compliance with conventional grid requirements: it curtailed power through LFSM-O during overfrequency conditions and injected 0.25 p.u. of reactive current during a fault ride-through (FRT) event at 1.129 p.u. voltage. In system split tests, the VSM absorbed surplus PV generation, stabilizing frequency after a transient rise to 52.8 Hz and containing voltage excursions beyond 1.2 p.u. During imbalance stress, it absorbed 1.266 MW against its 1.0 MW rating for approximately 2–3 s, corresponding to a 26.6% overload that falls within typical IGBT transient thermal capability but would require supervisory intervention (e.g., PV curtailment or load management) if sustained. These results demonstrate that while the PV inverter contributes valuable voltage support, only the grid-forming VSM maintains frequency stability and ensures secure islanded operation. The novelty of this study lies in integrating standardized compliance tests with system split scenarios, providing a comprehensive framework for evaluating grid-forming controls under both regulatory and resilience-oriented perspectives and informing the evolution of future grid codes.

Keywords: virtual synchronous machine (VSM); grid-forming inverter; grid-following photovoltaic inverter; system split and islanding; electromagnetic transient (EMT) simulation; converter-dominated grids; frequency; voltage stability

Academic Editor: Sérgio Cruz

Received: 5 January 2026
Revised: 5 February 2026
Accepted: 11 February 2026
Published: 15 February 2026

1. Introduction

The transition toward converter-dominated power systems has fundamentally altered the stability landscape of transmission and distribution networks [1]. Unlike synchronous machines, conventional converter-interfaced generation contributes little or no rotational inertia, which makes the system more sensitive to fast disturbances such as frequency ramps, voltage collapses, and islanding events [2,3]. Recent blackouts and near-miss incidents, including the Continental Europe system separation of 2006 [4], the South Australia blackout of 2016 [5], and the Texas 2021 winter event [6], have demonstrated the vulnerabilities of low-inertia systems.

Grid codes worldwide have evolved to mitigate these risks by mandating basic support functions such as frequency ride-through, fault ride-through (FRT), and limited frequency-sensitive modes [7,8]. In Europe, ENTSO-E defines compliance-oriented tests, while IEEE 1547-2018 and IEC 62786:2020 prescribe voltage and frequency support requirements for distributed energy resources (DERs) [9–11]. These frameworks secure fundamental grid stability but do not explicitly address system split resilience, leaving a critical gap in qualification procedures.

A fundamental distinction exists between grid-following (GFL) and grid-forming (GFM) control strategies. Grid-following inverters operate as controlled current sources that synchronize to the grid through Phase-Locked Loops (PLLs) [12]. While this allows accurate current injection under normal conditions, it renders them dependent on a strong grid reference and limits their ability to provide frequency or voltage support [13,14]. Their performance deteriorates under weak-grid conditions, and they typically disconnect during islanding or major disturbances. In contrast, grid-forming inverters behave as voltage sources that establish their own frequency and voltage references. This enables them to contribute synthetic inertia, enhance transient stability, provide black-start capability, and sustain autonomous operation during islanding [15,16]. As a result, GFMs are increasingly recognized as key enablers for the reliable operation of future converter-dominated grids.

Among the different grid-forming approaches, the Virtual Synchronous Machine (VSM) has received particular attention as it directly emulates the dynamics of synchronous generators by embedding the swing equation into the converter control loop [17,18]. This enables VSMs to provide synthetic inertia, damping, and frequency support in a way that is functionally comparable to traditional rotating machines [3]. Recent studies have demonstrated that VSM-based inverters can improve transient stability [19], enhance weak-grid operation [20], and coordinate effectively with conventional synchronous machines [21]. Large-scale research programs, including the EU MIGRATE project [22] and the UNIFI initiative [23], have benchmarked VSMs against other GFM controls under standardized testing protocols. Similarly, the framework developed by Kersic et al. [24] specifies the expected characteristics of grid-forming converters and provides detailed procedures for their validation. These initiatives have established a solid foundation for evaluating grid-forming controls under compliance-oriented conditions.

Nevertheless, compliance-oriented tests alone are insufficient to guarantee resilience. While they assess inertia response, LFSM, and FRT, they do not capture extreme system events such as abrupt phase-angle shifts and frequency excursions during system splits, where multiple stressors occur simultaneously [25]. Beyond the control algorithms themselves, accurate monitoring of grid parameters presents fundamental practical challenges. Matouš et al. [26] demonstrated in their study that galvanic isolation circuits, which are essential for voltage measurement, can introduce substantial signal distortion. Their findings revealed that total harmonic distortion varies considerably across different isolation methods, with changes ranging from −7.8% to 336.9%.

The observation that even conventional voltage transformers can significantly alter waveform fidelity underscores the importance of considering measurement chain imperfections when evaluating converter performance. While the present study focuses primarily on control algorithm resilience rather than measurement hardware characteristics, it is recognized that practical implementations require judicious selection of isolation methods to ensure accurate voltage feedback for both grid-following PLL synchronization and grid-forming voltage regulation. Addressing this gap requires complementary testing frameworks that extend beyond compliance and systematically evaluate inverter performance under resilience-oriented conditions.

The main contributions of this paper are summarized as follows:

- **Benchmark testing of the VSM:** A Virtual Synchronous Machine (VSM) was implemented and rigorously benchmarked against standardized protocols (Fraunhofer ISE, Kersic), including inertia response, LFSM-U, fault ride-through (FRT), and critical RoCoF [24,27]. The VSM delivered an equivalent inertia constant of $\sim$15 s, provided sustained LFSM-U support, injected reactive current during FRT, and maintained synchronization under $\pm$2 Hz/s RoCoF.
- **Testing of the PV inverter:** A grid-following photovoltaic (PV) inverter was evaluated against compliance-oriented functions. It curtailed active power via LFSM-O during overfrequency, injected reactive current during FRT, and supported voltage recovery. However, as expected for a GFL unit, it was unable to regulate frequency or sustain islanded operation.
- **System split and comparative analysis:** A novel islanding test case was developed to evaluate resilience beyond compliance. Results showed that while the PV inverter provided reactive voltage support, only the VSM maintained frequency stability and ensured secure islanded operation, even under overload stress.
- **Novelty:** While compliance test procedures exist in MIGRATE [28], UNIFI [23], Kersic et al. [24,27] and related frameworks, these verify performance under grid-connected conditions with a stiff external reference. A critical gap exists: converters passing all compliance tests may fail during system splits when the reference disappears entirely. This work provides three contributions: (i) a unified framework combining compliance and resilience testing within a single evaluation methodology; (ii) direct comparison of grid-forming and grid-following converters under identical disturbance sequences; and (iii) demonstration that compliance alone is insufficient—converters must be tested under islanding conditions to ensure resilience, thereby identifying qualification gaps that inform future grid code development.

2. Methodology

This study evaluates Virtual Synchronous Machines (VSMs) through two complementary steps. First, a benchmark feeder with a single VSM is tested under standardized scenarios to quantify core grid-forming properties. Second, a mixed feeder with a VSM and a grid-following (GFL) PV inverter is used to assess resilience during system splits.

Both cases are implemented in the electromagnetic transient (EMT) domain using DIgSILENT PowerFactory 2025, which provides a detailed representation of converter dynamics and grid interactions, developed by DIgSILENT GmbH, Gomaringen, Germany.

Rating Basis Summary

Two test configurations are employed: (i) benchmark compliance tests (Section 3) using a 20 MVA VSM where per-unit values such as 0.545 p.u. and 0.61 p.u. represent 54.5% and 61% of the rated capacity respectively—well within continuous operating limits—and (ii) system split resilience tests (Section 5) using a 1.15 MVA VSM and PV inverter at the

distribution scale, where the observed 1.266 MW absorption represents a 26.6% transient overload above the 1.0 MW dispatch.

The VSM's DC side was modeled as an ideal voltage source; in practice, the modest energy requirements for synthetic inertia (∼4 kWh for benchmark tests) and transient overload (∼0.2 kWh for system split) would be supplied by co-located battery storage or supercapacitors.

Table 1 lists the abbreviations used throughout this paper, and Table 2 defines the nomenclature. Table 3 summarizes the rating basis for key results.

Table 1. List of abbreviations.

Abbreviation	Definition
DER	Distributed Energy Resource
DSL	DIgSILENT Simulation Language
EMT	Electromagnetic Transient
ENTSO-E	European Network of Transmission System Operators for Electricity
FRT	Fault Ride-Through
GFL	Grid-Following
GFM	Grid-Forming
IGBT	Insulated-Gate Bipolar Transistor
LFSM-O	Limited Frequency-Sensitive Mode–Overfrequency
LFSM-U	Limited Frequency-Sensitive Mode–Underfrequency
LV	Low Voltage
MV	Medium Voltage
PCC	Point of Common Coupling
PHIL	Power Hardware-in-the-Loop
PLL	Phase-Locked Loop
PV	Photovoltaic
RoCoF	Rate of Change of Frequency
SCR	Short-Circuit Ratio
TSO	Transmission System Operator
VSM	Virtual Synchronous Machine

Table 2. Nomenclature.

Symbol	Description	Unit
H	Inertia constant	s
J	Virtual moment of inertia	kg·m^2
D_p	Damping coefficient	p.u.
D_q	Reactive-power droop coefficient	p.u./p.u.
K_p	Active-power–frequency droop	%
ω	Angular frequency	rad/s
ω_0	Nominal angular frequency	rad/s
θ	Rotor/voltage angle	rad
P	Active power	W or p.u.
Q	Reactive power	var or p.u.
P_{ref}	Active-power reference	p.u.
V	Voltage magnitude	V or p.u.
E	Internal EMF magnitude	p.u.
I	Current magnitude	A or p.u.
R_v	Virtual resistance	p.u.
X_v	Virtual reactance	p.u.
f	Frequency	Hz

Table 2. *Cont.*

Symbol	Description	Unit
f_0	Nominal frequency (50 Hz)	Hz
S_{base}	Base apparent power	MVA

Table 3. Rating basis for reported results.

Test	Section	VSM Rating	Peak Value	Status
Inertia response	Section 3.5.1	20 MVA	0.545 p.u. (10.9 MW)	Normal operation (54.5%)
LFSM-U	Section 3.5.2	20 MVA	0.61 p.u. (12.2 MW)	Normal operation (61%)
Critical RoCoF	Section 3.5.4	20 MVA	0.55–0.60 p.u.	Normal operation
System split	Section 5.1.4	1.0 MW	1.266 MW	Transient overload (126.6%)

3. VSM Benchmark Distribution Grid

3.1. System Description

A benchmark feeder was developed in DIgSILENT PowerFactory to evaluate the grid-forming capabilities of a standalone Virtual Synchronous Machine (VSM). The test setup, shown in Table 4, consists of a 20 MVA VSM inverter dispatched at 5 MW with unity power factor, connected at the Point of Common Coupling (PCC). The feeder is energized by a 20 kV three-phase grid simulator, interfaced through a 3 MVA series reactor ($R = 0.15\,\Omega$, $X = 1.5\,\Omega$) and a controllable breaker that emulates the upstream transmission system. A general load is connected downstream of the PCC to provide realistic power exchange conditions.

This setup is used for standardized testing of grid-forming converters, including evaluation of voltage source behavior, inertial response under active-power disturbances, and fault ride-through capability. The corresponding schematic is shown in Figure 1.

Table 4. Parameters of the VSM benchmark system.

Parameter	Value
VSM Converter	
Rated apparent power	20 MVA
Dispatch setpoint	5 MW (0.25 p.u.)
Power factor	Unity
Virtual inertia constant H	15 s
Damping coefficient D_p	40 p.u.
P–f droop	5%
Grid Simulator	
Voltage	20 kV, 3-phase
Frequency	50 Hz (programmable)
Short-circuit capacity	≈120 MVA
Series Reactor	
Rating	3 MVA
Resistance R	0.15 Ω
Reactance X	1.5 Ω
X/R ratio	10
Network Conditions	
SCR at PCC	≈6
Breaker	Controllable PCC disconnection
Load	Generic PCC load (variable)

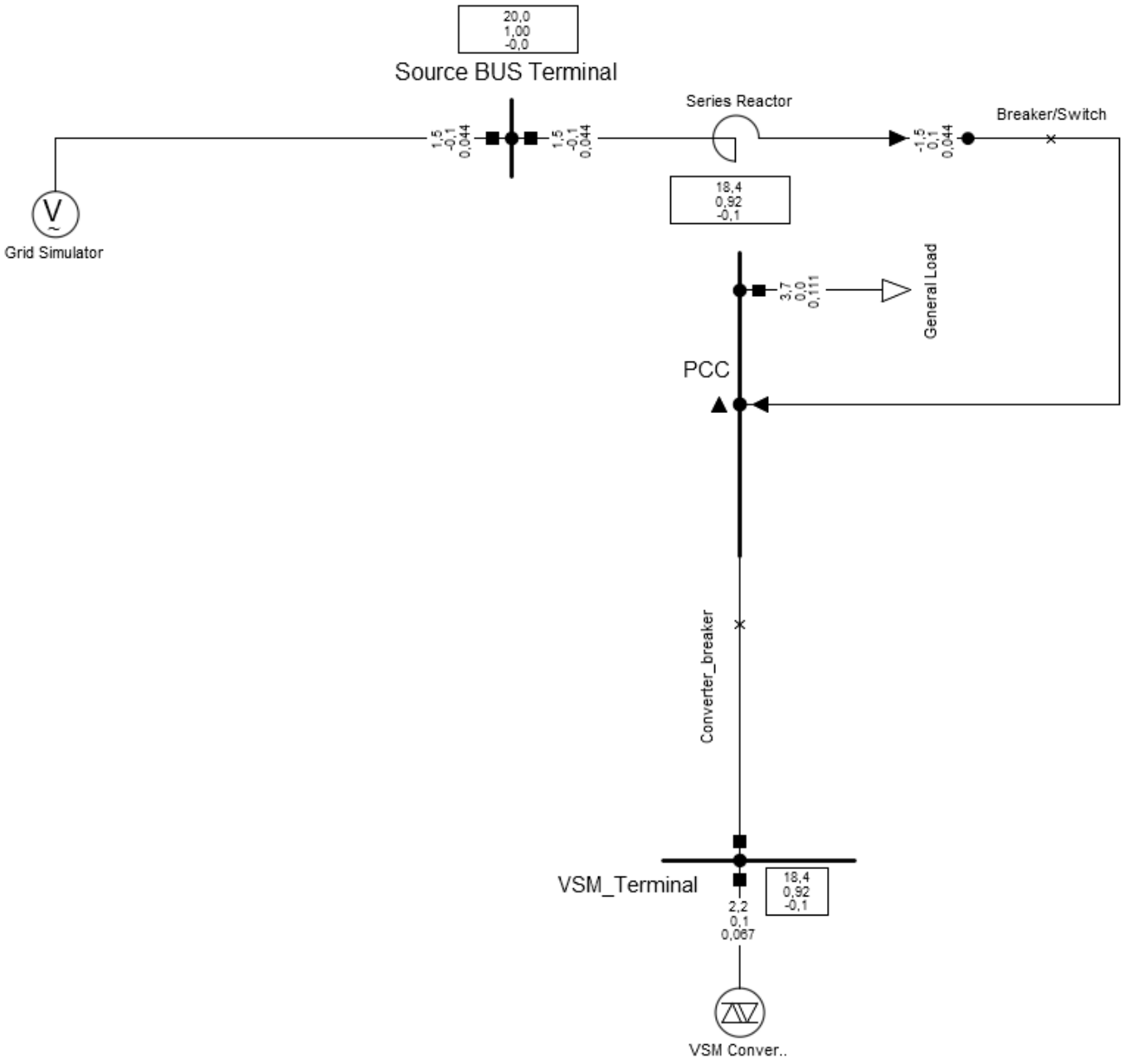

Figure 1. Schematics of the VSM benchmark distribution grid.

3.2. Virtual Synchronous Machine (VSM) Control

The Virtual Synchronous Machine (VSM) is a grid-forming control strategy that emulates the electromechanical dynamics of a synchronous generator [29]. Its main objective is to provide synthetic inertia, damping, and autonomous voltage–frequency support, ensuring stable operation in converter-dominated grids [30].

3.2.1. Swing Equation Representation

At the core of the VSM lies the swing equation, which governs the rotor dynamics of synchronous machines and is reproduced by the converter. In torque form, the dynamics are written as

$$J\frac{d\omega}{dt} = T_m - T_e - D_d(\omega - \omega_0), \qquad T = \frac{P}{\omega} \tag{1}$$

where J is the virtual inertia constant, ω the instantaneous angular frequency, ω_0 the nominal angular frequency, P_{ref} the reference active power, P the measured active power, and D_d the damping coefficient in torque units. Expressing the swing equation in terms of power gives

$$J\frac{d\omega}{dt} = \frac{P_{\text{ref}} - P}{\omega_0} - D_d(\omega - \omega_0). \tag{2}$$

This ensures consistent physical units [N m].

Alternatively, in per-unit form (commonly used in power system analysis), the swing equation is

$$2H\,\frac{d\Delta\omega}{dt} = P_{\text{ref}} - P - D_p\,\Delta\omega, \qquad \Delta\omega = \frac{\omega - \omega_0}{\omega_0}. \tag{3}$$

where H is the inertia constant in seconds and D_p is the per-unit damping coefficient.

The rotor angle is obtained by integrating the frequency:

$$\frac{d\theta}{dt} = \omega. \tag{4}$$

This formulation enables the VSM to reproduce inertial response and oscillation damping similar to a synchronous machine.

It is important to distinguish between the control emulation and physical energy delivery: The swing equation in ((2)–(4)) constitutes a control algorithm that computes the required active-power reference based on measured frequency deviation. This computed reference is then realized physically through the inverter's inner current control loops, which modulate the PWM switching to inject or absorb the commanded power. The energy for this power exchange is supplied by the DC-side storage element (battery or supercapacitor connected to the DC-link). Thus, the 'virtual inertia' is virtual only in the sense that no rotating mass exists, which means that the energy exchange is real and must be supported by adequate DC-side energy capacity.

3.2.2. Governor and Active-Power–Frequency Droop

Primary frequency regulation is introduced through a governor mechanism that adjusts the power reference denoted as P_{ref} according to frequency deviation:

$$P_{ref} = P_{set} - K_p(\omega - \omega_{set}), \tag{5}$$

where P_{set} is the scheduled active power, ω_{set} the frequency setpoint, and K_p the droop coefficient. This allows the VSM to share frequency control in proportion to load deviations, mimicking the behavior of conventional governors.

3.2.3. Reactive-Power–Voltage Droop Control

Voltage regulation is achieved through a Q–V droop law that adapts the internal voltage magnitude to reactive-power exchange:

$$E = V_{ref} - D_q(Q - Q_{set}), \tag{6}$$

where E is the generated internal voltage, V_{ref} the reference voltage, Q the measured reactive power, Q_{set} the scheduled reactive setpoint, and D_q the reactive droop constant.

All the above equations about frequency and voltage droop can be seen in Figure 2 below.

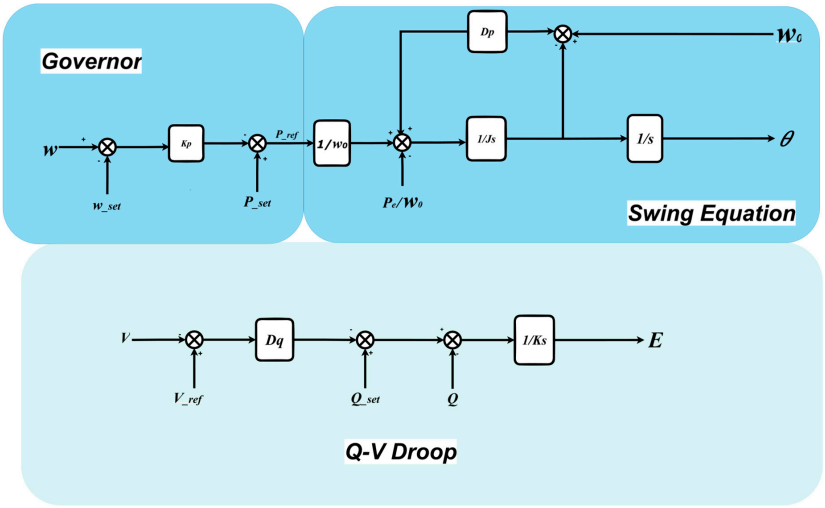

Figure 2. Virtual synchronous machine control with active-power–frequency and reactive-power–voltage droop dynamics.

3.2.4. Control Architecture and Features

The overall VSM architecture consists of three main elements: (i) a governor loop enforcing P–f droop (5), (ii) the swing equation block capturing inertia and damping (2)–(4), and (iii) the Q–V droop controller (6).

Together, these blocks enable the VSM to reproduce the key attributes of synchronous machines, namely: synthetic inertia and damping, autonomous frequency and voltage support, fault ride-through capability, and stable islanded operation.

During power injection (underfrequency response), energy is drawn from the DC-side storage through the inverter to the AC grid. During power absorption (overfrequency or islanded surplus conditions), the power flow reverses, with energy stored in the DC-side element; this energy injection and absorption are depicted in Figure 3. The DC-link was modelled as an ideal voltage source in this study; practical implementations would size the energy storage based on the quantified requirements: approximately 4 kWh for benchmark inertia tests and 0.2 kWh for system split transient overload.

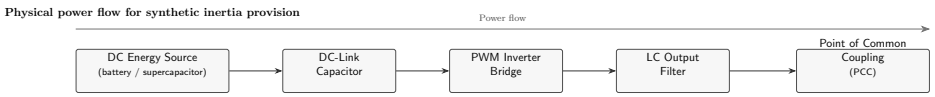

Figure 3. Energy flow path: The physical power flow for synthetic inertia provision.

3.3. Implementation in PowerFactory

In DIGSILENT POWERFACTORY, the VSM was implemented as a composite model linking the canonical Equations (2)–(6) with measurement and interface blocks suitable for EMT simulations. This structure ensures that the theoretical control dynamics are directly reproduced in a form applicable to standardized testing and system split studies.

DIgSILENT Simulation Language (DSL) Implementation

The internal dynamics were programmed in PowerFactory's DSL using interdependent control layers:

- **Swing equation core**: inertia J, damping D_p, and frequency/angle tracking.
- **Governor action**: active-power–frequency droop for primary regulation.
- **Voltage-dependent power limiting**: reduces P_{ref} under low-voltage conditions.
- **Stabilizing filters**: lead–lag and low-pass filtering on P, Q, and ω for EMT stability.
- **Overload protection**: corrective frequency shift $\Delta\omega_{\text{ol}}$ for ride-through.

- **Reference** : generates (θ) generated to set frequency and phase.

This layered implementation allows the VSM to replicate synchronous machine behavior while ensuring numerical stability in EMT simulations. It provides a robust framework for benchmarking and resilience analysis in converter-dominated grids.

3.4. Standardized Testing Protocol

To validate the VSM implementation against emerging international standards, a series of standardized test cases was defined. The methodology follows the Fraunhofer ISE Grid-Forming Benchmark Procedures [27] and the Kersic guidelines [24] on grid-forming converter characteristics, providing reproducible and hardware-relevant frameworks.

The selected tests capture essential grid-forming properties:

- **Fault ride-through (FRT):** evaluates stability during voltage dips and post-fault recovery in both grid-connected and islanded modes.
- **Voltage source properties:** assesses whether the VSM establishes a stiff terminal voltage, including impedance shaping and setpoint tracking.
- **Inertial response:** quantifies the synthetic inertia contribution through the swing equation under applied frequency deviations.
- **Overload conditions:** examines current limiting and overload protection functions.
- **Combined event:** superimposes multiple disturbances (e.g., fault and load step) to test coordinated response and recovery.

Together, these tests reflect the core grid-forming attributes and also establish a rigorous benchmark for the implemented VSM, and enable fair comparison with the grid-following PV inverter.

3.5. Standardized Testing Results and Discussions

3.5.1. Inertia Response Test

The inertia contribution of the Virtual Synchronous Machine (VSM) was evaluated by subjecting it to a controlled frequency ramp applied through the grid simulator as seen in Figure 4. Prior to the disturbance, the converter was operating steadily at approximately 0.25 p.u. active power. At $t = 2$ s, the active-power setpoint was increased to $P_{\text{set}} = 0.30$ p.u. This preloading step is intentional: it ensures the VSM operates at a stable non-zero baseline, enabling the inertial burst governed by the swing term $J\,d\omega/dt$ to manifest as a clear deviation around the scheduled operating point.

At $t = 4$ s, the system frequency was reduced linearly from 50 Hz to 48.5 Hz, corresponding to a rate of change of frequency (RoCoF) of approximately $|\dot{f}| = 0.4$ Hz/s. In response, the VSM delivered a transient-power surge. The active power rose from its preloaded value of 0.30 p.u. to a peak of

$$P_{\text{pk}} \approx 0.545 \text{ p.u.},$$

A corresponding increase in converter current was also recorded, consistent with the transient-power injection.

There is an inertial headroom, relative to the scheduled preloaded output, of

$$\Delta P = P_{\text{pk}} - P_{\text{set}} = 0.245 \text{ p.u.}.$$

The corresponding per-unit frequency slope is

$$|\dot{\omega}_{\text{pu}}| = \frac{|\dot{f}|}{f_0} = \frac{0.4}{50} = 8 \times 10^{-3} \text{ s}^{-1},$$

and applying the swing relation

$$\Delta P \approx 2H\,|\dot{\omega}_{\mathrm{pu}}|$$

yields an equivalent inertia constant of

$$H = \frac{\Delta P}{2\,|\dot{\omega}_{\mathrm{pu}}|} = \frac{0.245}{0.016} \approx 15.31 \text{ s}.$$

On a 20 MVA base, this corresponds to a stored kinetic energy of

$$E_k = H \cdot S_{\mathrm{base}} \approx 15.31 \times 20 = 306.3 \text{ MJ},$$

and an equivalent virtual inertia of

$$J_{\mathrm{virt}} = \frac{2HS_{\mathrm{base}}}{(2\pi f_0)^2} \approx 6.21 \times 10^3 \text{ kg·m}^2.$$

These results confirm that the VSM effectively provides synthetic inertia. The controller injects active power proportional to the imposed RoCoF magnitude, thereby supporting the system frequency during the decline, and subsequently returns smoothly to the scheduled operating point without instability or current-limit violations.

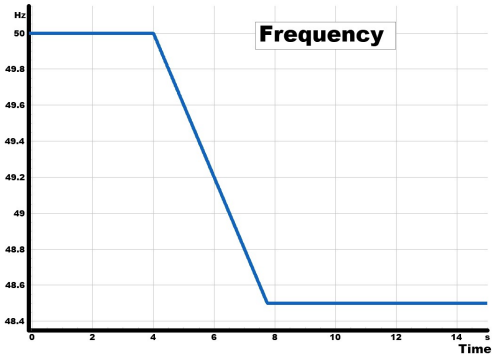

(**a**) Frequency trajectory (50 Hz → 48.5 Hz).

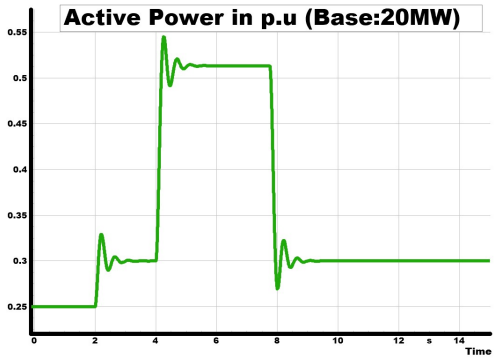

(**b**) VSM active power response.

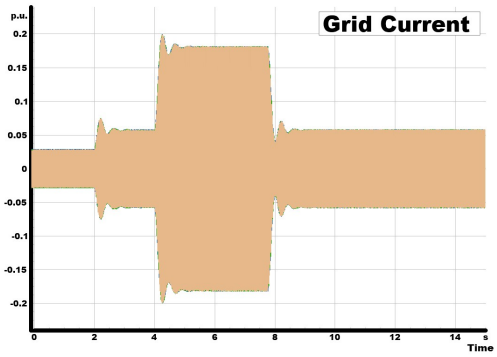

(**c**) Grid-phase currents at PCC.

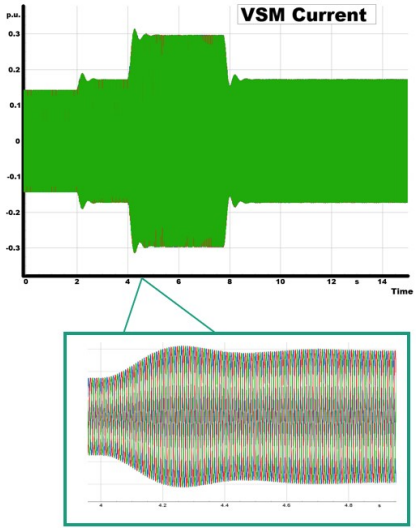

(**d**) VSM converter-phase currents.

Figure 4. Inertia response of the VSM to a programmed frequency ramp. The VSM injects additional active power during the negative RoCoF (inertial support), with a proportional rise in converter current, and settles back toward the scheduled operating point after the ramp.

The equivalent inertia constant $H \approx 15\,\text{s}$ represents a control parameter in the swing equation that is mathematically independent of operating point or DC-side conditions. The swing equation consistently computes the required power response as $\Delta P = 2H\left|\frac{d\omega}{dt}\right|$ regardless of PV loading level. However, the effective delivery of this computed response may be constrained by:

1. Converter current limits, which may clip the response during severe RoCoF events;
2. DC-side energy availability, where finite storage capacity limits sustained power exchange;
3. Available power headroom, which decreases as the VSM approaches rated capacity.

For the test conditions employed (VSM at 30% loading, ideal DC source), these constraints did not limit the observed inertial response. Future work should systematically vary these parameters to map the operational envelope.

3.5.2. Inertia Response with LFSM-U Test

The setup mirrors the inertia-only case: a linear ramp from 50 Hz to 48.5 Hz starts at $t = 4$ s, and the VSM is preloaded to $P_{\text{set}} = 0.30$ p.u. at $t = 2$ s. In line with ENTSO-E, LFSM-U triggers below 49.8 Hz and increases active power in proportion to the frequency shortfall, sustained for the event duration.

Control Law Implemented

The LFSM-U function activates when frequency falls below the threshold $f_2 = 49.8$ Hz, increasing active power proportionally to the frequency shortfall:

$$\Delta P_U = S_{droop} \cdot (f_n - f)^+, \quad f < f_2 \tag{7}$$

where $S_{droop} = 0.05$ p.u./Hz and $(x)^+ = \max(x, 0)$. The output is subject to amplitude limiting ($\Delta P_{max} = 0.10$ p.u.) and slew-rate limiting to prevent abrupt power changes. This signal is added to the swing equation reference, enabling the VSM to provide both inertial response (proportional to $d\omega/dt$) and sustained droop support (proportional to Δf). The complete DSL implementation details are provided in Appendix A.

Observed Behavior and Compliance

From Figure 5, it can be observed that as the frequency f declined, the VSM first delivered the inertial burst $M_{\text{vsm}}\dot{\omega}$, lifting power to ≈0.545 p.u. When f crossed 49.8 Hz, LFSM-U engaged and the sustained droop raised output to 0.60–0.62 p.u. at 48.5 Hz. With `droop` = 5 %/Hz (i.e., $S_{\text{droop}} = 0.05$ p.u./Hz), a 1.5 Hz shortfall gives $\Delta P_U^{\star} = 0.05 \times 1.5 = 0.075$ p.u.; after the amplitude/slew limits and the $T_{\texttt{smooth}} = 0.02$ s filter, this settles to the measured 0.06–0.07 p.u.

The two ENTSO-E points which are accurate trigger at 49.8 Hz and sustained support, of which both are satisfied.

3.5.3. Fault Ride-Through (FRT) and Islanding Test

This test evaluated the behavior of the VSM under a combined short-circuit and islanding event. At $t = 0.5$ s, a three-phase fault was applied at the PCC, reducing the grid-side voltage from about 1.0 p.u. to 0.7 p.u. The fault was cleared at $t = 1.0$ s, allowing the external grid voltage to recover to nominal. During the fault, the upstream breaker was opened at $t = 0.7$ s, isolating the feeder and leaving the VSM as the sole grid-forming source.

The results show that the VSM maintained sinusoidal and stable terminal voltage despite the external short-circuit, while the grid voltage exhibited a clear sag. Once the

breaker opened, the VSM seamlessly transitioned into islanded operation, autonomously establishing the local voltage reference. Grid currents rose sharply during the fault, peaking at about ±0.5 p.u., but collapsed to zero immediately after disconnection. In contrast, the VSM current continued supplying the load, confirming a smooth and uninterrupted transition from grid-connected to islanded mode.

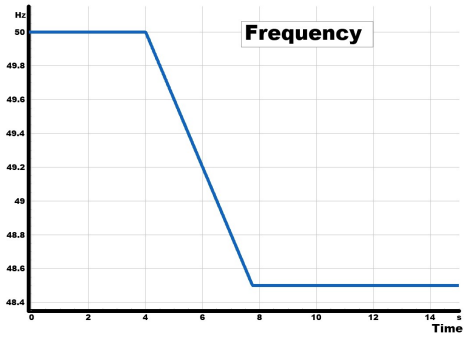

(**a**) Frequency trajectory (50 Hz → 48.5 Hz, LFSM-U threshold at 49.8 Hz).

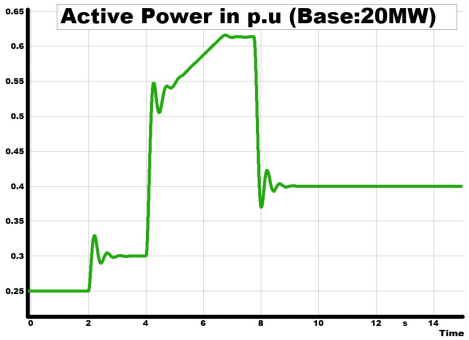

(**b**) VSM active power response with LFSM-U.

(**c**) Grid-phase currents at PCC.

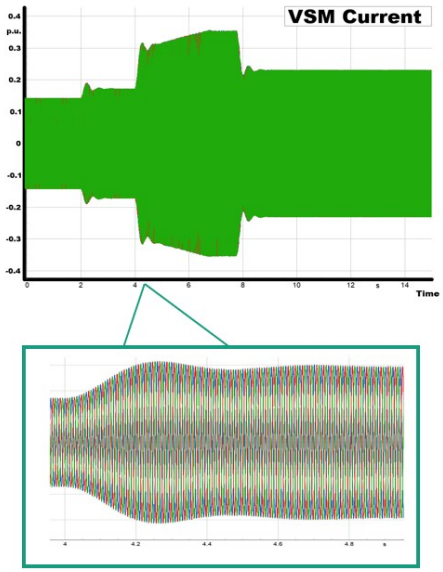

(**d**) VSM converter-phase currents.

Figure 5. The VSM injects extra power during negative RoCoF using synthetic inertia and continues power injection after crossing the LFSM-U threshold (49.8 Hz), with an increase in current.

Figure 6 shows that the reactive-power dynamics highlight the supportive behavior of the controller. During the fault, the VSM injected reactive current, with reactive power rising rapidly to approximately 1.2–1.3 p.u., consistent with fault ride-through requirements. After islanding, the reactive power decayed and stabilized around 0.8 p.u., reflecting the balance dictated by the islanded load and voltage regulation objectives.

These results confirm that the VSM remained stable and compliant during a severe grid disturbance and sustained independent operation after separation. This demonstrates the robustness of grid-forming control, providing both fault ride-through support and reliable islanding performance.

3.5.4. Critical RoCoF Test

This test investigated the performance of the VSM under severe frequency transients using a predefined sequence of ramps and hold phases. The schedule began with an initial 20 s steady operation at 50 Hz, followed by a ramp at -2 Hz/s down to 48 Hz, a short hold, and a subsequent return to 50 Hz at $+2$ Hz/s. The profile then included a further ramp to 52 Hz, a sustained hold, and finally a -2 Hz/s ramp back to nominal frequency. This sequence imposed alternating RoCoFs of up to ± 2 Hz/s with stabilization intervals at 48, 50, and 52 Hz, representing a critical stress case for converter-dominated systems.

The results in Figure 7 confirm that the VSM maintained synchronism throughout the entire profile. During negative RoCoFs, the converter injected additional active power, reaching peaks of about 0.55–0.60 p.u., while during positive RoCoFs it absorbed power, dipping to approximately 0.05–0.10 p.u. Active power then returned smoothly to its 0.30 p.u. setpoint without sustained oscillations, demonstrating good damping of inertial bursts.

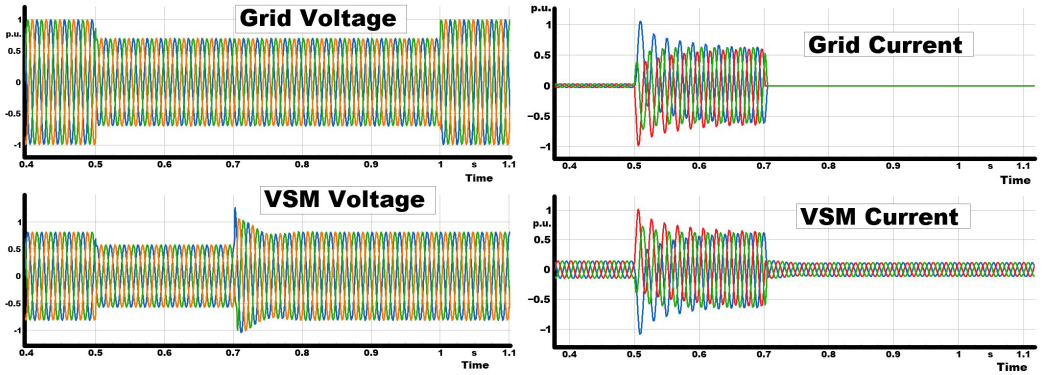

(**a**) Grid and VSM voltages. (**b**) Grid and VSM currents.

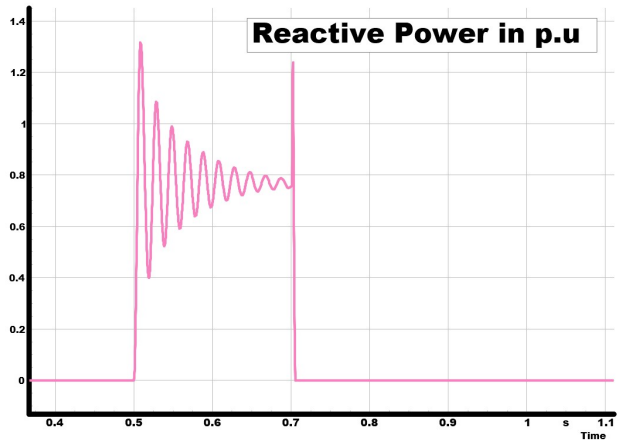

(**c**) Reactive power during fault ride-through and islanding.

Figure 6. VSM performance during fault ride-through (FRT) and islanding. (**a**) The VSM maintains sinusoidal voltage despite a short circuit and after grid disconnection. (**b**) Grid current collapses after islanding, while VSM current sustains the load. (**c**) Reactive-power injection supports FRT and stabilizes in islanded mode.

Current measurements further support this behavior. As shown in Figure 7c, both grid and VSM phase currents remained sinusoidal, with amplitude increasing during steep ramps but remaining within ± 0.4 p.u., indicating that current limits were not violated. The VSM therefore delivered synthetic inertia and RoCoF support without compromising stability or incurring excessive current stress.

This test demonstrates that the VSM can withstand critical RoCoFs of ± 2 Hz/s while preserving synchronization, providing proportional inertial support, and respecting current

constraints. This confirms the suitability of grid-forming control for challenging dynamic conditions in low-inertia systems.

Current measurements show that both grid and converter currents remained sinusoidal and within rated limits, even during the steepest ramps. The rise in current amplitude was effectively constrained by the implemented virtual impedance and overload-limiter functions, ensuring stability and avoiding protective triggers.

Overall, the VSM demonstrated robust synthetic inertia performance under RoCoFs of up to ± 2 Hz/s, maintaining stable operation and current compliance across all phases. These results underline the capability of VSM-based control to handle severe frequency disturbances, thereby meeting one of the key resilience requirements for grid-forming inverter qualification.

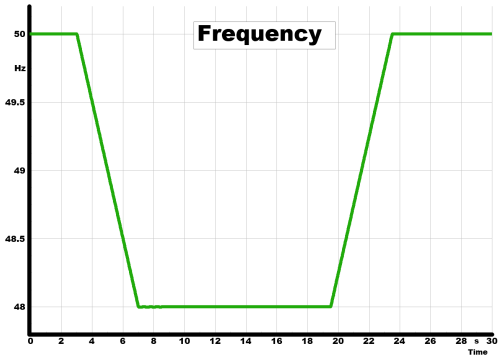

(**a**) Frequency trajectory for the critical RoCoF schedule (Procedure 2): ramps of $\pm$ 2 Hz/s with holds at 48, 50, and 52 Hz.

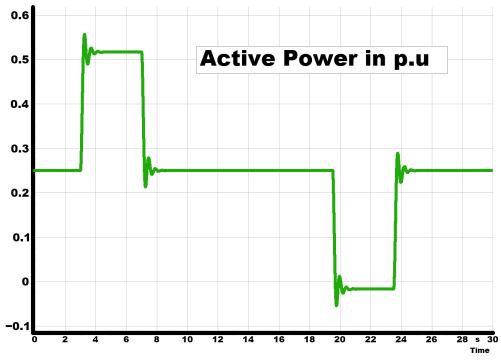

(**b**) VSM active power: inertial bursts proportional to RoCoF and well-damped recovery to the setpoint after each ramp.

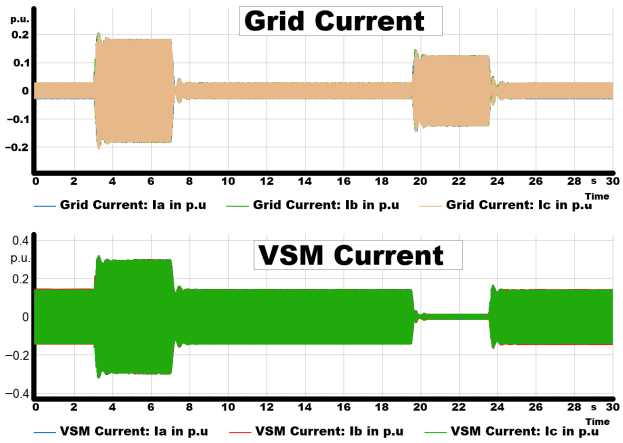

(**c**) Currents: grid and VSM phase currents remain sinusoidal; amplitude rises during steep ramps but stays within limits.

Figure 7. Critical RoCoF performance of the VSM under $\pm$ 2 Hz/s frequency ramps. The converter sustains synchronization, provides virtual inertia, and respects current limits across all phases.

3.5.5. Combined Event: Phase-Angle Change and RoCoF

This test examined the robustness of the VSM under a combined disturbance consisting of a sudden phase-angle shift followed by staged RoCoF events. At $t = 10$ s, the grid's phase angle was abruptly shifted from 0° to -20°, representing the type of phase jump that can occur during system split events. Immediately after this disturbance, the grid frequency was varied according to which introduced successive RoCoF stages with both positive and negative ramps as well as short hold periods.

The results in Figure 8 demonstrate the layered response of the VSM. Figure 8a shows that despite the −20° phase-angle step, the VSM rapidly re-synchronized with the shifted reference and stabilized the frequency during the following RoCoF ramps, preventing sustained deviation from nominal. Figure 8b highlights the active-power dynamics: the VSM injected additional power during the frequency decline, with power rising by approximately 0.25 to 0.30 p.u. above the baseline before smoothly settling as the frequency stabilized.

Current behavior provides further evidence of resilience. The grid current, shown in Figure 8c, rose sharply during the disturbance, with peaks approaching 0.8 p.u., but returned to steady levels once the VSM counteracted the imbalance. Importantly, the converter current in Figure 8d remained well within its rated envelope throughout the event, indicating that the VSM supplied the required support without experiencing overloading.

This combined test confirms that the VSM can withstand simultaneous angular and frequency disturbances without loss of synchronism or violation of current limits. Such resilience is critical for system split scenarios, where multiple stressors often occur together rather than in isolation, and highlights the capability of the grid-forming control to sustain stability under compounded disturbances.

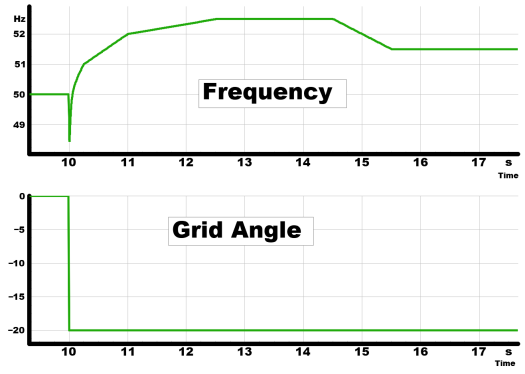

(**a**) Frequency response during the phase-angle and RoCoF disturbance.

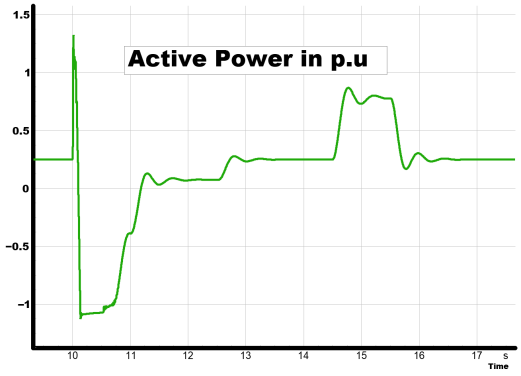

(**b**) VSM active power response during disturbance.

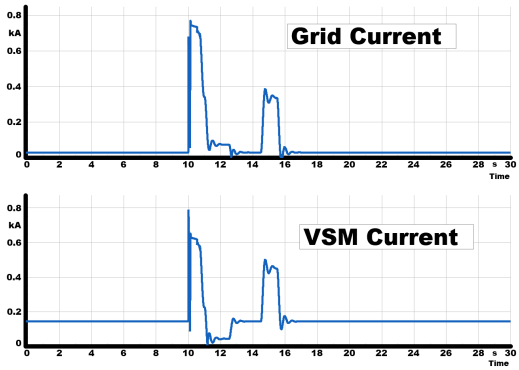

(**c**) Grid current during the phase-angle and RoCoF disturbance, and (**d**) VSM current during the disturbance.

Figure 8. Combined event results: (**a**) frequency response, (**b**) VSM active power, (**c**) grid current, and (**d**) VSM current during the phase-angle and RoCoF disturbance. The VSM converter maintains grid support by injecting active power and ensuring stable current delivery.

4. System Split Case with VSM and PV Inverter

4.1. System Description

The second configuration introduces a grid-following (GFL) PV inverter alongside the VSM, creating a mixed-resource feeder representative of converter-dominated grids. The PV unit is rated at 1.15 MVA (1.0 MW dispatch, unity power factor) and connected at the 0.4 kV side of a 2.5 MVA, 0.4/20 kV Dyn step-up transformer. It is modeled as a current-controlled inverter synchronized through a Phase-Locked Loop (PLL).

In parallel, a 1.15 MVA VSM inverter operates as the grid-forming source. During normal operation, the external grid defines the system voltage and frequency. A system split is emulated by opening the upstream breaker, which isolates the feeder into an island powered solely by the VSM and PV inverter.

The network provides a short-circuit ratio (SCR) of approximately 6–7 at the PCC with an X/R ratio of 10, representative of medium-voltage distribution feeders. The series reactor ($R = 0.15\ \Omega$, $X = 1.5\ \Omega$) emulates upstream impedance with unity zero-sequence ratios. The Dyn11 transformer with solidly grounded LV neutral provides a ground reference for the island. Prior to the split at $t = 3$ s, both converters operate at the unity power factor with combined generation exceeding local load by 20–50%, creating a surplus that the VSM must absorb post-split.

This setup enables direct comparison between the two control paradigms during islanding. The analysis focuses on frequency stability, voltage regulation, and continuity of supply when the system relies entirely on converter-based resources. The schematic of this configuration is shown in Figure 9.

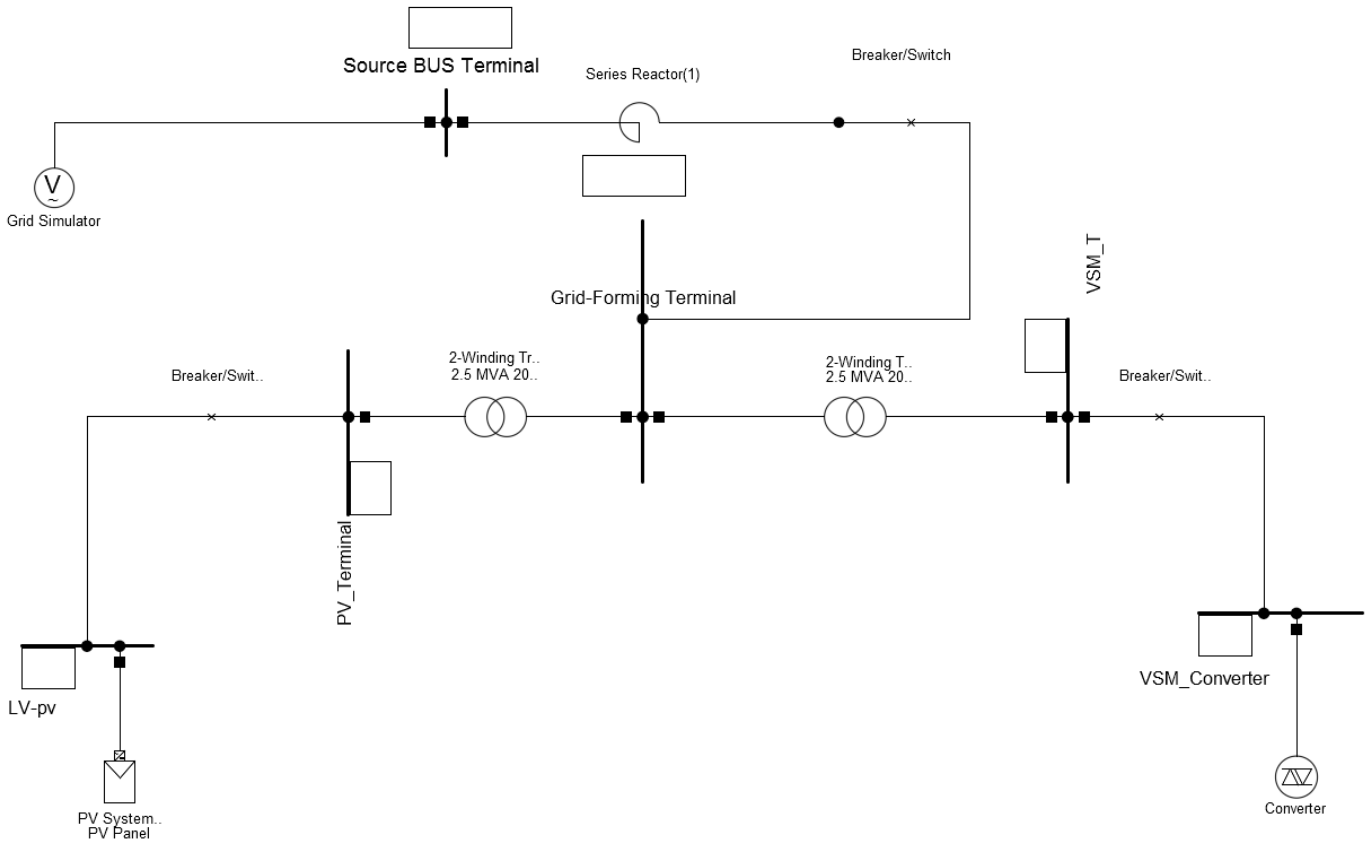

Figure 9. System split with VSM and grid-following PV.

4.2. Grid-Following PV Inverter Control

The grid-following photovoltaic (PV) inverter was implemented using the standard DIgSILENT PowerFactory library model, ensuring consistency with established benchmark practices and reproducibility. To allow a fair comparison with the VSM, the default control parameters were adapted in line with ENTSO-E grid code requirements and the objectives of this study.

The implemented inverter follows a conventional grid-following (GFL) control structure, where synchronization is achieved through a Phase-Locked Loop (PLL) that aligns the converter with the external voltage phase. The main functionalities are:

- **PLL-based synchronization:** tracks grid phase and frequency for current injection in synchronism with the grid voltage.
- **Low-voltage fault ride-through (FRT):** injects reactive current during voltage dips, supporting post-fault voltage recovery in accordance with ENTSO-E requirements.
- **Limited frequency-sensitive mode (LFSM-O):** reduces active-power output proportionally during overfrequency events, contributing to primary frequency control.
- **Current limitation and power curtailment:** enforces operational limits and prevents overcurrent conditions.

Figure 10 illustrates the control architecture, showing the interaction of PLL synchronization, power control, FRT, LFSM-O, and current limiting.

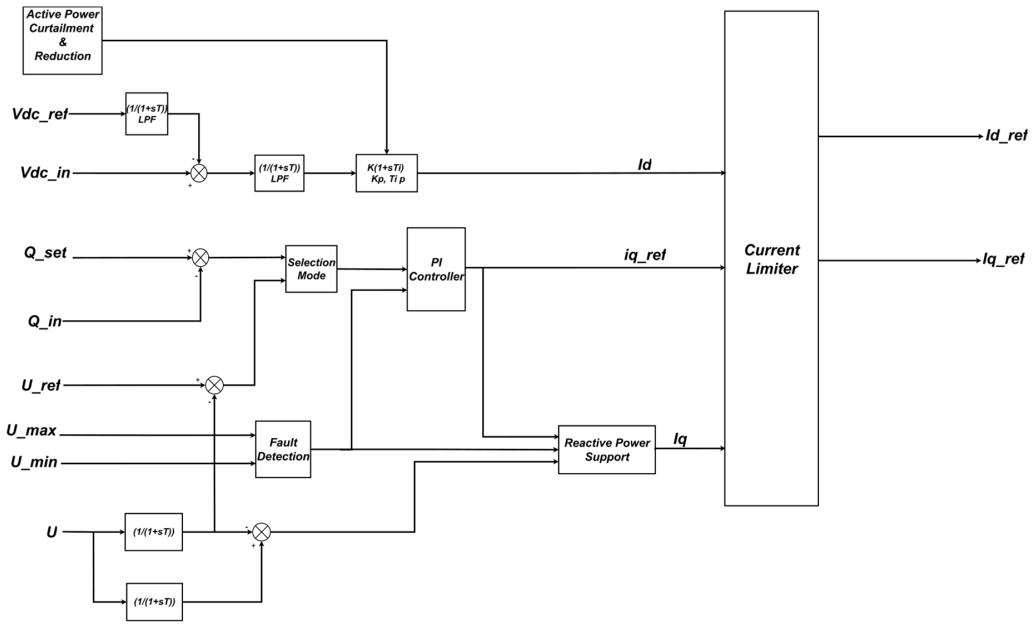

Figure 10. Simplified control structure of the grid-following PV inverter, including PLL synchronization, power control, LFSM-O, FRT, and current limitation.

5. Results and Discussion

This section presents and discusses the simulation results obtained from the PV system grid-following and system split tests, which are implemented in DIgSILENT PowerFactory (Gomaringen, Germany).

5.1. PV Inverter Implementation Parameters

The PV inverter was implemented using the DIgSILENT PowerFactory standard "Photovoltaic System" template from the Global Library. Table 5 documents all modified parameters.

The PV inverter was configured with standard SRF-PLL synchronization. While enhanced weak-grid modes (reduced-bandwidth PLL, power synchronization) can improve

GFL stability under degraded conditions, they cannot address the fundamental limitation demonstrated here: a current-source converter cannot establish voltage and frequency references when the external grid disappears entirely. This architectural constraint, rather than controlling tuning, represents the core GFL/GFM distinction that motivates our comparative analysis.

Table 5. Parameters of the VSM–PV system split configuration.

Parameter	Value
VSM Inverter	
Rated power	1.15 MVA (1.0 MW dispatch)
Inertia constant H	15 s
Damping coefficient D_p	40 p.u.
Virtual impedance $R_v + jX_v$	$0.09 + j0.09$ p.u.
Over-current threshold	1.01 p.u.
LFSM-U threshold/droop	49.8 Hz/0.05 p.u./Hz
PV Inverter	
Rated power	1.15 MVA (1.0 MW dispatch)
PLL bandwidth/damping	20 Hz/0.707
FRT gain K_{FRT}	2
LVRT/HVRT threshold	0.9/1.91 p.u.
Max. current	1.1 p.u.
LFSM-O threshold	50.2 Hz
Network	
Transformer	2.5 MVA, Dyn11, grounded LV
Series impedance	$0.15 + j1.5\ \Omega$ ($X/R = 10$)
SCR at PCC	≈6–7

We acknowledge that modern grid-following inverters with fast frequency response (FFR) capability can provide valuable frequency support during grid-connected operation. Our findings should not be interpreted as dismissing this contribution. Rather, we emphasize that such support is contingent on the presence of an external grid reference. In mixed systems containing both GFL and GFM converters, the complementary roles are clear: GFL units with FFR can reduce the burden on GFM units during frequency excursions, while GFM units provide the essential voltage–frequency reference that enables GFL units to function. Neither capability substitutes for the other.

5.1.1. LFSM-O Test of the PV Inverter

Before assessing the full system split scenario, the standalone grid-following (GFL) PV inverter was validated under the limited frequency-sensitive mode–overfrequency (LFSM-O) function. According to ENTSO-E requirements, LFSM-O is triggered once the system frequency exceeds 50.2 Hz, leading to a proportional reduction in active power output.

Figure 11 illustrates the inverter's response. As the grid frequency rose above the 50.2 Hz threshold, the PV inverter curtailed its active-power output in proportion to the deviation. The reduction was stepwise and proportional, with power falling from the initial operating level of approximately 2.5–3.0 MW toward zero as the frequency reached its maximum excursion above 52 Hz. The frequency rise was thereby moderated, and the inverter maintained synchronism and stable operation throughout the event.

This confirms that the implemented PV inverter complies with ENTSO-E specifications for frequency support under overfrequency conditions. The LFSM-O function was correctly triggered at the prescribed threshold, applied proportional active-power curtailment, and

remained stable without oscillations or instability. The inverter configuration is therefore validated and suitable for subsequent comparative analysis with the VSM in the system split scenarios.

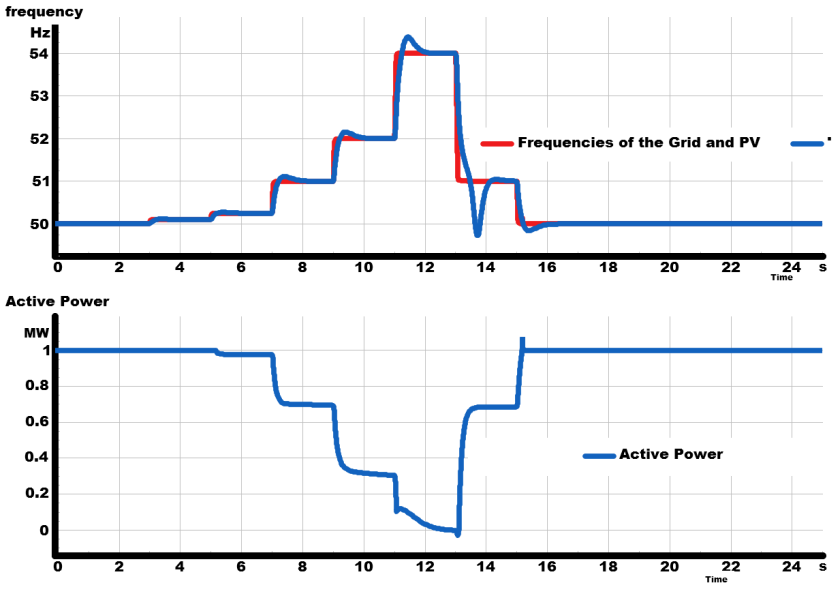

Figure 11. LFSM-O test of the grid-following PV inverter. The inverter curtails active power once the frequency rises above the 50.2 Hz threshold, ensuring compliance with ENTSO-E requirements.

5.1.2. Fault Ride-Through (FRT) Test of the PV Inverter

In addition to frequency support, the PV inverter was validated for fault ride-through (FRT) under overvoltage conditions. When the terminal voltage exceeds a threshold V_{th} (here $V_{\text{th}} = 1.10$ p.u.), the reactive current reference follows a proportional droop law,

$$i_{q,\text{ref}} = \begin{cases} k\,(V - V_{\text{th}}), & V > V_{\text{th}}, \\ 0, & V \le V_{\text{th}}, \end{cases} \tag{8}$$

where k is the overvoltage reactive current gain (droop coefficient, in p.u./p.u.).

In the observed event, the measured peak voltage was

$$V = 1.129 \text{ p.u.} \quad \Rightarrow \quad \Delta V \equiv V - V_{\text{th}} = 1.129 - 1.10 = 0.029 \text{ p.u.}. \tag{9}$$

Equivalently, when referenced to nominal ($V_{\text{nom}} = 1.0$ p.u.),

$$\Delta V_{\text{nom}} \equiv V - V_{\text{nom}} = 1.129 - 1.0 = 0.129 \text{ p.u.}. \tag{10}$$

With a configured droop coefficient of $k = 2$, the theoretical reactive current command is

$$i_{q,\text{ref}} = k\,\Delta V_{\text{nom}} = 2 \times 0.129 = 0.258 \text{ p.u.} \quad \text{(referenced to nominal)}, \tag{11}$$

$$\text{or} \quad i_{q,\text{ref}} = k\,\Delta V = 2 \times 0.029 = 0.058 \text{ p.u.} \quad \text{(referenced to the 1.10 p.u. threshold)}. \tag{12}$$

Figure 12 shows that the inverter injected approximately 0.25 p.u. of reactive current, in close agreement with (11). At the same time, the inverter curtailed active power to remain within current limits. The response was prompt when V exceeded 1.10 p.u. and was sustained until the voltage returned toward nominal, demonstrating effective overvoltage support and compliance with FRT requirements.

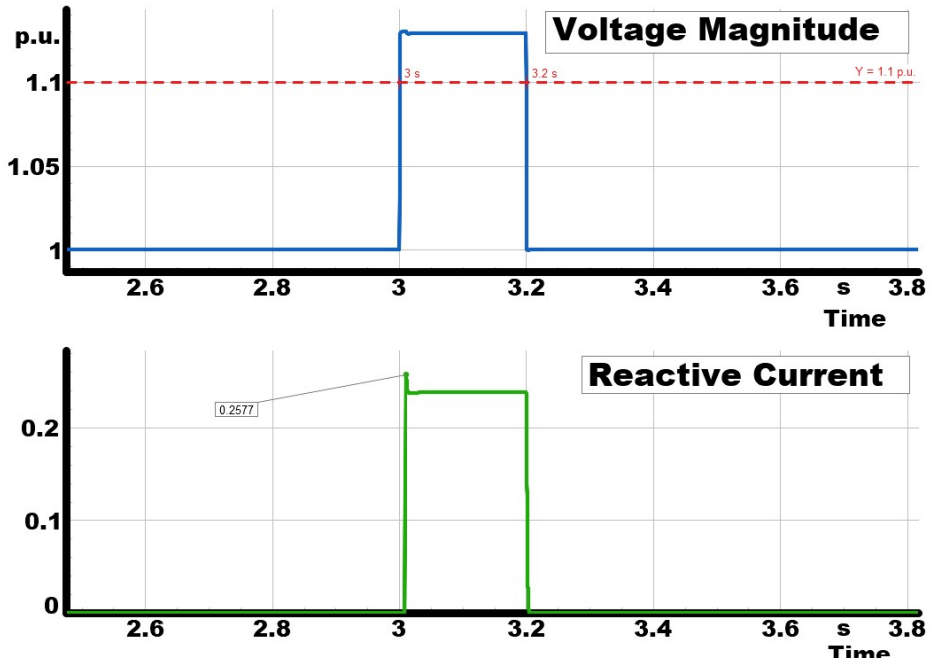

Figure 12. FRT test of the grid-following PV inverter. The inverter injects reactive current according to the droop law when the grid voltage exceeds 1.1 p.u., reaching $i_{q,ref} = 0.258$ p.u. and supporting voltage recovery.

5.1.3. System Split Test: Island Test

The resilience of the mixed system under islanding was assessed through a system split test. At $t = 3$ s, the upstream breaker was opened, disconnecting the feeder from the main grid. Before the disconnection, both the VSM and the PV inverter were synchronized to the external grid and delivering active power.

Once the grid was disconnected, the operating conditions changed abruptly. The VSM was forced to establish the local voltage and frequency reference, while also absorbing the surplus active power generated by the PV inverter. As shown in Figure 13, this imbalance triggered a rapid frequency rise that peaked at approximately 52.8 Hz before being stabilized by the VSM. In parallel, Figure 13 shows a voltage excursion above 1.2 p.u., which activated the PV inverter's reactive current injection. The PV delivered about 0.25 p.u. of reactive current in proportion to the deviation, providing valuable voltage support.

The active-power dynamics are shown in Figure 13: while the PV continued to inject active power, the VSM rapidly shifted its output negative, absorbing the surplus generation to counterbalance the mismatch. This action damped the frequency excursion and restored stability around the islanded load demand.

The system split test reveals the distinct and complementary roles of the two converter types. The PV inverter (grid-following) contributed to voltage stability through a reactive current injection of approximately 0.25 p.u., proportional to voltage deviation, as governed by its FRT droop characteristic (Equation (8)). However, being a current-source device synchronized via PLL, it inherently cannot regulate frequency or establish a voltage reference, these functions require an external grid or grid-forming source. In contrast, the VSM (grid-forming) autonomously established the island's voltage and frequency reference, absorbed the surplus PV generation through its swing equation dynamics, and stabilized the system after a transient frequency rise to 52.8 Hz. This test confirms that while PV-driven reactive support aids voltage recovery, only VSM-driven active-power–frequency control can ensure stable islanded operation.

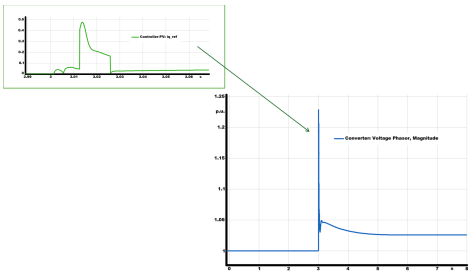

(**a**) Voltage and reactive current response during system split.

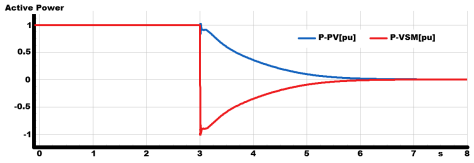

(**b**) Active-power response during system split.

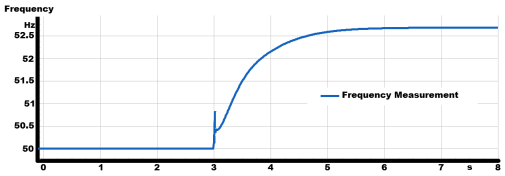

(**c**) Frequency response following grid disconnection.

Figure 13. System behavior during the split test, showing voltage, power, and frequency dynamics.

The term 'secure islanded operation' refers specifically to the VSM's ability to maintain system stability during the critical transient period (first 2–5 s) following grid disconnection. During this phase, the VSM absorbs surplus generation through its swing equation dynamics, containing frequency excursions within acceptable limits. For sustained island operation beyond this transient period, the elevated frequency (52.8 Hz) automatically engages the PV inverter's LFSM-O function, which curtails active power once frequency exceeds 50.2 Hz. This frequency-driven curtailment mechanism provides the energy balance required for continuous operation. Additional supervisory measures which include coordinated load shedding and energy storage dispatch would further enhance long-term island stability as detailed in Section 6.2.

5.1.4. Power Imbalance During Island Mode and Converter Stress

The impact of active-power imbalance during islanded operation was assessed in a scenario where the PV system was rated at 1.5 MW, while the grid-forming VSM converter had a nominal capacity of 1.0 MW. Following the system split, the VSM was required to absorb the excess generation from the PV. As shown in Figure 14, this resulted in an absorbed power of approximately 1.266 MW.

The overload can be quantified relative to the nominal converter rating as follows:

$$\frac{P_{\text{abs}}}{P_{\text{rated}}} = \frac{1.266}{1.0} = 1.266 \quad \Rightarrow \quad 26.6\% \text{ overload.} \tag{13}$$

Such overloading places considerable stress on the converter's semiconductor devices and thermal management system, leading to increased junction temperatures, accelerated device aging, and reduced long-term reliability. Although the VSM successfully stabilized frequency and voltage in the short term, sustained operation under this condition would be unsafe.

These results explain the importance of supervisory strategies to prevent prolonged overloads. Possible approaches include curtailing PV generation, implementing fast-acting demand-side management, or diverting surplus power into local energy storage. Keeping the VSM within its rated limits is essential not only for immediate stability but also for protecting the converter's lifetime and ensuring reliable long-term operation.

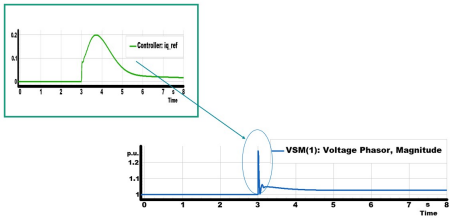

(**a**) Voltage and reactive current response during system split.

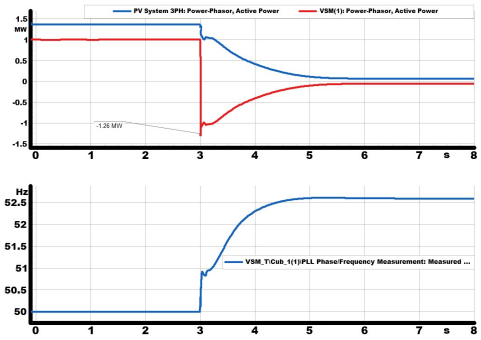

(**b**) Active-power response during system split.

Figure 14. Active power absorption of the GFM during islanded operation, showing exceedance of rated limits.

From a compliance perspective, it should be noted that while ENTSO-E grid codes explicitly require frequency support functions such as LFSM-U and fault ride-through capability, they do not mandate overload absorption beyond converter ratings. Therefore, system-level supervisory control is indispensable to ensure that generation and demand remain balanced in islanded operation without exposing the VSM to sustained overstress.

The interaction between PV power injection and VSM absorption is bounded by the following mechanism: As the VSM absorbs surplus PV generation, its swing equation dynamics cause frequency to rise. When frequency exceeds 50.2 Hz, the PV inverter's LFSM-O function activates, reducing PV output proportionally (droop of 5%/Hz per ENTSO-E requirements). This creates a negative feedback loop: higher frequency $\rightarrow$ reduced PV injection $\rightarrow$ reduced VSM absorption requirement $\rightarrow$ frequency stabilization. For the tested configuration (PV: 1.5 MW, VSM: 1.0 MW), the transient overload of 26.6% lasted 2–3 s before LFSM-O curtailment reduced the imbalance. The thermal limit for this overload duration, based on typical IGBT junction temperature-rise characteristics, is approximately 2–5 s for a 25–30% overload, confirming that the observed response falls within safe transient operating limits.

5.2. Practical Acceptability of Observed Excursions

The observed excursions fall within acceptable transient limits. The 52.8 Hz frequency peak (+5.6% deviation) lasted less than 1 second before VSM regulation restored it within bounds; overfrequency protection with typical 100–500 ms delay would not trip. The voltage excursion beyond 1.2 p.u. lasted approximately 0.5–1 s, within short-duration withstand capability. The 26.6% power overload implies $\sim$60% increased losses ($P_{loss} \propto I^2$), sustainable for 2–5 s based on typical IGBT thermal characteristics; the 2–3 s observed duration falls within this window. In deployment, supervisory control would intervene via LFSM-O curtailment (activating above 50.2 Hz), load shedding, or storage dispatch.

6. Conclusions

This study provided an in-depth evaluation of Virtual Synchronous Machines (VSMs) operating as grid-forming inverters in converter-dominated power systems. Two complementary case studies were performed in DIgSILENT PowerFactory: a standalone benchmark feeder and a mixed feeder subjected to a system-splitting disturbance.

The benchmark simulations confirmed that the VSM reliably emulated the dynamic behavior of a synchronous machine. It delivered synthetic inertia (with an effective $H \approx 15$ s) during rapid frequency changes, supplied sustained active power via LFSM-U in line

with ENTSO-E specifications, and remained stable even under severe RoCoF conditions ($\pm$2 Hz/s). Furthermore, the VSM exhibited robust fault ride-through performance and preserved independent voltage and frequency control during islanded operation.

The system split scenario underlined the distinct yet complementary functions of grid-forming and grid-following converters. The PV inverter (GFL) met the LFSM-O and FRT criteria and provided reactive-power support during voltage deviations. However, once the external grid reference was lost, it was unable to sustain stable operation. In contrast, the VSM (GFM) established the island, redefined the voltage–frequency reference, absorbed excess PV generation and maintained continuity of supply, undergoing only a short controlled overload (26.6% for 2–3 s), which remained within typical transient thermal limits of IGBTs.

6.1. Recommendations for Grid Code Development

Based on our findings, we propose the following modifications and complementary additions to existing frameworks.

ENTSO-E Requirements for Generators (RfG)—Proposed Enhancements

The current Commission Regulation (EU) 2016/631 provides comprehensive requirements for grid connection. However, based on system split resilience testing, we recommend the following complementary provisions.

Enhanced Fault Ride-Through (Related to Article 13)

- **Recommendation**: Extend fault ride-through requirements to explicitly include "island ride-through" capability, which means the ability to transition to stable islanded operation if a fault results in system separation.
- **Rationale**: Current FRT requirements focus on remaining connected during faults with eventual grid restoration, but do not explicitly address the case where the fault leads to permanent system separation.
- **Gap Addressed**: System split events demonstrated that converters passing standard FRT tests may still fail during islanding scenarios.

Synthetic Inertia Quantification (Complementary to Article 15)

- **Recommendation**: Specify minimum equivalent inertia constant (e.g., $H \geq 5$ s) with standardized RoCoF test verification for grid-forming units.
- **Rationale**: While Article 15(2)(c) addresses LFSM-U (frequency-sensitive mode for underfrequency), explicit synthetic inertia requirements with quantified H values and standardized testing procedures would provide clearer performance benchmarks.
- **Gap Addressed**: Current requirements specify frequency response but do not mandate specific inertial performance metrics.

Island Operation Capability (Complementary to Article 16)

- **Recommendation**: Make island operation capability mandatory for grid-forming units (Type C and D power park modules) with defined test procedures.
- **Rationale**: Article 15(5)(b) makes island operation capability optional ("if required by the relevant system operator"), but system split testing demonstrates this is a critical resilience function.
- **Gap Addressed**: The optional nature of island operation in current regulations means many grid-forming units may not be tested for this critical capability.

IEEE 1547-2018—Proposed Enhancements

Intentional Islanding Category (Related to Clause 8.2)

- **Recommendation**: Add enhanced specifications within Category III or create supplementary requirements for DERs specifically designed for intentional island operation.
- **Current Status**: Clause 8.2 addresses intentional islanding but does not create a distinct performance category.
- **Proposed Enhancement**: Establish clear performance benchmarks distinguishing DERs capable of autonomous island formation and stabilization from those only capable of participating in pre-established islands.
- **Gap Addressed**: Current standard permits intentional islanding but does not distinguish between passive island participation and active island formation capabilities.

Inertial Response Requirements (Related to Clause 6.5.2.8)

- **Recommendation**: Require grid-forming DERs to demonstrate inertial response (proportional to df/dt) as a mandatory function in addition to frequency-droop response.
- **Current Status**: IEEE 1547-2018 Clause 6.5.2.8 defines inertial response as an optional capability.
- **Proposed Enhancement**: Make inertial response mandatory for DERs designated as grid-forming, with specific performance metrics (e.g., minimum H equivalent, maximum response time).
- **Gap Addressed**: Distinction between frequency droop (proportional to Δf) and inertial response (proportional to df/dt) is not clearly mandated.

Proposed System Split Resilience Test

To address the gap between compliance testing and operational resilience, we propose a standardized system split qualification test:

Pre-Conditions

- Grid connection via impedance giving SCR = 3–10.
- Converter operating at 30–70% loading.
- Generation-load mismatch of $\pm$20–50%.

Procedure

1. Establish stable grid-connected operation.
2. Open upstream breaker to simulate system separation.
3. Monitor system behavior for a minimum of 60 s.

Pass Criteria

- Frequency stabilizes within $\pm$2.5 Hz within 5 s.
- Voltage remains within 0.85–1.15 p.u. after 1 s transient.
- Continuous energization maintained throughout the test period.
- No protection system false trips or instability.

Rationale

This test complements existing compliance tests by evaluating performance under the specific conditions of system separation, where multiple stressors (phase-angle jumps, frequency excursions, voltage transients, power imbalances) occurring simultaneously.

6.2. Recommendations for Supervisory Control

6.2.1. Fast Generation Curtailment

- LFSM-O response time should be minimized (<200 ms) to reduce grid-forming converter overload duration during overfrequency islands.
- Coordinate curtailment actions across multiple generation sources within the island.

6.2.2. Pre-Planned Load Shedding

- Island-capable feeders should have automated underfrequency load shedding coordinated with grid-forming converter droop settings.
- Establish clear priority levels for load disconnection.

6.2.3. Energy Storage Integration

- Co-located storage can absorb transient imbalances more rapidly than generation curtailment, reducing grid-forming converter stress.
- Size storage to handle expected maximum imbalance for 5–10 s (bridge to supervisory control activation).

6.3. Limitations and Future Work

This study is based on EMT simulations that have been validated against recognized benchmark frameworks. Additional experimental validation using Power Hardware-in-the-Loop (PHIL) or Hardware-in-the-Loop (HIL) testing would further enhance confidence in the results, especially in relation to protection coordination, thermal performance, and real-time control implementation. PHIL-based validation is highlighted as a key objective for future research.

PV variability effects: The PV generation was treated as quasi-static in this study to isolate control behavior and align with standardized benchmark protocols. Future work would incorporate realistic irradiance-driven variability profiles (e.g., cloud transients with ramp rates of 10–50%/s) to assess the impact of PV fluctuations on VSM headroom requirements and islanded frequency resilience. Such studies would quantify the additional inertia or storage capacity needed to accommodate PV variability under islanded conditions.

Additional future directions include:

- Multi-VSM coordination with heterogeneous inertia constants
- Parametric sensitivity studies across SCR, load levels, and control parameters
- Integration of detailed thermal models for overload duration assessment
- Hybrid GFM/GFL control strategies for enhanced weak-grid operation

6.4. Important Note on Regulatory Framework References

The recommendations above are proposed enhancements based on observed system behavior during resilience testing. They reference existing articles in ENTSO-E RfG and IEEE 1547-2018 to provide context, but **do not claim these specific provisions currently exist in the standards**. Implementation of these recommendations would require:

1. Stakeholder consultation processes as specified in the relevant regulations;
2. Cost–benefit analysis to justify enhanced requirements;
3. Coordination with national regulatory authorities;
4. Development of standardized testing protocols;
5. Consideration of technology-specific limitations and capabilities.

Author Contributions: Conceptualization, H.S. and A.S.; Methodology, I.O.L. and H.S.; Validation, I.O.L.; Formal analysis, I.O.L. and H.S.; Investigation, H.S.; Resources, A.S.; Writing—original draft,

I.O.L.; Writing—review & editing, H.S. and A.S.; Supervision, H.S. and A.S. All authors have read and agreed to the published version of the manuscript.

Funding: This research received no external funding.

Data Availability Statement: The original contributions presented in this study are included in the article. Further inquiries can be directed to the corresponding authors.

Conflicts of Interest: The authors declare no conflict of interest.

Appendix A. LFSM-U Implementation Details

This appendix provides the complete DSL implementation of the LFSM-U function described in Section 3.5.2.

Appendix A.1. Control Law Definitions

Let f be the measured frequency, $f_n = 50$ Hz, $f_2 = 49.8$ Hz. The LFSM-U droop parameter entered as `droop` in %/Hz is converted to

$$S_{\text{droop}} = \frac{\texttt{droop}}{100} \quad \text{(p.u./Hz)}, \qquad (x)_+ = \max(x, 0) \tag{A1}$$

Appendix A.2. Activation Gate (Piecewise)

$$u_U(f) = \begin{cases} 1, & f < f_2 \\ 0, & f \geq f_2 \end{cases} \tag{A2}$$

Appendix A.3. Gated Droop Request (Unlimited)

$$\Delta P_U^* = u_U(f) \cdot S_{\text{droop}} \cdot (f_n - f)_+ \tag{A3}$$

Appendix A.4. Amplitude Limit

$$\Delta P_{U,\text{lim}} = \text{sat}_{[0,\Delta P_{\max}]}(\Delta P_U^*) \tag{A4}$$

Appendix A.5. Slew Limit

Let $x = (\Delta P_{U,\text{lim}} - \Delta P_U)/T_\epsilon$, with ramp limits $\ddot{P}_{U,\min}$ and $\ddot{P}_{U,\max}$:

$$\dot{\Delta P}_U = \begin{cases} \ddot{P}_{U,\min}, & x < \ddot{P}_{U,\min} \\ x, & \ddot{P}_{U,\min} \leq x \leq \ddot{P}_{U,\max} \\ \ddot{P}_{U,\max}, & x > \ddot{P}_{U,\max} \end{cases} \tag{A5}$$

Appendix A.6. Smoothing Filter (PT1)

$$T_{\text{smooth}} \dot{dP} + dP = \Delta P_{\text{FSM}} + \Delta P_{\text{LFSM-O}} + \Delta P_U, \quad T_{\text{smooth}} = 0.02 \text{ s} \tag{A6}$$

Appendix A.7. Plant Reference

$$P_{\text{ref}} = P_{\text{set}} + M_{\text{vsm}} \dot{\omega} + dP, \quad \omega = 2\pi f \tag{A7}$$

References

1. Saleh, A.M.; István, V.; Khan, M.A.; Waseem, M.; Ali Ahmed, A.N. Power system stability in the Era of energy Transition: Importance, Opportunities, Challenges, and future directions. *Energy Convers. Manag. X* **2024**, *24*, 100820. [CrossRef]
2. He, C.; Geng, H.; Rajashekara, K.; Chandra, A. Analysis and Control of Frequency Stability in Low-Inertia Power Systems: A Review. *IEEE/CAA J. Autom. Sin.* **2024**, *11*, 2363–2383. [CrossRef]
3. Saeedian, M.; Pournazarian, B.; Seyedalipour, S.S.; Eskandari, B.; Pouresmaeil, E. Emulating Rotational Inertia of Synchronous Machines by a New Control Technique in Grid-Interactive Converters. *Sustainability* **2020**, *12*, 5346. [CrossRef]
4. van der Vleuten, E.; Lagendijk, V. Transnational infrastructure vulnerability: The historical shaping of the 2006 European "Blackout". *Energy Policy* **2010**, *38*, 2042–2052. [CrossRef]
5. Yan, R.; Masood, N.A.; Kumar Saha, T.; Bai, F.; Gu, H. The Anatomy of the 2016 South Australia Blackout: A Catastrophic Event in a High Renewable Network. *IEEE Trans. Power Syst.* **2018**, *33*, 5374–5388. [CrossRef]
6. Bell, K.; Hawker, G.; UKERC. Preparing for a Resilient Energy Future: Learning from Texas' Rolling Blackouts. 2021. Available online: https://ukerc.ac.uk/news/preparing-for-a-resilient-energy-future-learning-from-texas-rolling-blackouts/ (accessed on 1 January 2026).
7. Zeb, K.; Islam, S.U.; Khan, I.; Uddin, W.; Ishfaq, M.; Curi Busarello, T.D.; Muyeen, S.; Ahmad, I.; Kim, H. Faults and Fault Ride Through strategies for grid-connected photovoltaic system: A comprehensive review. *Renew. Sustain. Energy Rev.* **2022**, *158*, 112125. [CrossRef]
8. Rodrigues, J.; Moreira, C.; Lopes, J.P. Fault-Ride-Through Approach for Grid-Tied Smart Transformers without Local Energy Storage. *Energies* **2021**, *14*, 5622. [CrossRef]
9. ENTSO-E. ENTSO-E Requirements for Generators—Interpretation. 2016. Available online: https://www.entsoe.eu/network_codes/rfg/ (accessed on 1 January 2026).
10. *IEEE 1547-2018*; Introduction to IEEE 1547 Standard for Interconnecting Distributed Energy Resources with Electric Power Systems. IEEE Standards Association: Piscataway, NJ, USA, 2023. Available online: https://www.sandia.gov/app/uploads/sites/273/2023/11/2023_Vermont_Webinar_Vartanian1.pdf (accessed on 1 January 2026).
11. Ilija, I.; Paul, W.; Wanda, A.; EASY-SRI. Report on the Contribution to Standardization. 2024. Available online: https://www.easysri.eu/en/Project%20Results%20%20Documents/D6.6%20Report%20on%20the%20contribution%20to%20standardization%20v1.pdf (accessed on 1 January 2026).
12. Geng, S.; Hiskens, I.A. Unified Grid-Forming/Following Inverter Control. *IEEE Open Access J. Power Energy* **2022**, *9*, 489–500. [CrossRef]
13. Chatterjee, D. From Grid Following to Grid Forming: Modeling, Control and Applications to Inverter-Based Resources. Master's Thesis, The University of Texas, Austin, TX, USA, 2022. [CrossRef]
14. Liu, Y.; Zhu, L.; Xu, X.; Li, D.; Liang, Z.; Ye, N. Transient Synchronization Stability in Grid-Following Converters: Mechanistic Insights and Technological Prospects—A Review. *Energies* **2025**, *18*, 1975. [CrossRef]
15. Lasseter, R.H.; Chen, Z.; Pattabiraman, D. Grid-Forming Inverters: A Critical Asset for the Power Grid. *IEEE J. Emerg. Sel. Top. Power Electron.* **2020**, *8*, 925–935. [CrossRef]
16. Ahmed, F.; Al Kez, D.; McLoone, S.; Best, R.J.; Cameron, C.; Foley, A. Dynamic grid stability in low carbon power systems with minimum inertia. *Renew. Energy* **2023**, *210*, 486–506. [CrossRef]
17. Shadoul, M.; Ahshan, R.; AlAbri, R.S.; Al-Badi, A.; Albadi, M.; Jamil, M. A Comprehensive Review on a Virtual-Synchronous Generator: Topologies, Control Orders and Techniques, Energy Storages, and Applications. *Energies* **2022**, *15*, 8406. [CrossRef]
18. Unruh, P.; Nuschke, M.; Strauß, P.; Welck, F. Overview on Grid-Forming Inverter Control Methods. *Energies* **2020**, *13*, 2589. [CrossRef]
19. Chen, Z.; Yao, J.; He, W.; Luo, Y.; Xie, H.; Zou, Z. Transient stability enhancement control strategy based on grid dispatching for multi-paralleled grid forming inverters during LVRT. *Int. J. Electr. Power Energy Syst.* **2024**, *157*, 109836. [CrossRef]
20. Villada-Leon, C.A.; Posada Contreras, J.; Rosas-Caro, J.C.; Núñez-Rodríguez, R.A.; Valencia, J.C.; Valdez-Resendiz, J.E. Control Algorithm for an Inverter-Based Virtual Synchronous Generator with Adjustable Inertia. *Eng* **2025**, *6*, 231. [CrossRef]
21. Alassi, A.; Feng, Z.; Ahmed, K.; Syed, M.; Egea-Alvarez, A.; Foote, C. Grid-forming VSM control for black-start applications with experimental PHiL validation. *Int. J. Electr. Power Energy Syst.* **2023**, *151*, 109119. [CrossRef]
22. MIGRATE. MIGRATE – Massive Integration of Power Electronic Devices. 2018. Available online: https://der-lab.net/wp-content/uploads/2018/11/Munzel_MIGRATE_at_IRED_2018-%E2%80%93.pdf (accessed on 1 January 2026).
23. Kroposki, B.; National Renewable Energy Laboratory (NREL). UNIFI Specifications for Grid-Forming Inverter-Based Resources: Version 2. 2024. Available online: https://docs.nrel.gov/docs/fy24osti/89269.pdf (accessed on 1 January 2026).
24. Kersic, M.; Müller, T.; Lewis, E.; Schaupp, T.; Denninger, R.; Ernst, P.; Reichert, S.; Rogalla, S.; Singer, R.; Ise, T.; et al. Testing Characteristics of Grid-Forming Converters—Part I: Specification and Definition of Behaviour. 2020. Available online: https://www.researchgate.net/publication/349041906_Testing_Characteristics_of_Grid_Forming_Converters_Part_I_Specification_and_Definition_of_Behaviour (accessed on 1 January 2026).

25. Dsilva, S.; Zare, A.; Shadmand, M.B.; Bayhan, S.; Abu-Rub, H. Towards resiliency enhancement of network of grid-forming and grid-following inverters. *IEEE Trans. Ind. Electron.* **2024**, *71*, 1547–1558. [CrossRef]
26. Matouš, H.; Libra, M.; Poulek, V.; Kouřím, P. Analysis of Output Signal Distortion of Galvanic Isolation Circuits for Monitoring the Mains Voltage Waveform. *Sensors* **2022**, *22*, 7769. [CrossRef]
27. Rogalla, S.; Greulich, A.; Lehner, J.; Lens, H.; Ernst, P.; Schaupp, T.; Singer, R.; Ungerland, J.; Schöll, C.; Denninger, R.; et al. Grid-forming converters in interconnected systems—final results from the joint research project VerbundnetzStabil. In Proceedings of the 20th International Workshop on Large-Scale Integration of Wind Power into Power Systems as well as on Transmission Networks for Offshore Wind Power Plants (WIW 2021), Berlin, Germany, 29–30 September 2021; pp. 135–140. [CrossRef]
28. Denis, G.; Prevost, T. *MIGRATE D3.6: Requirement Guidelines for Operating a Grid with 100% Power Electronic Devices*; Réseau de Transport d'Électricité (RTE): Paris, France, 2019. [CrossRef]
29. Quintero-Durán, M.J.; Candelo-Becerra, J.E.; González-Niño, M.E.; Hernández-Moreno, S.A.; Váz, R.F. Synchronverter Control Strategy: A Review of Different Improvements and Applications. *Energies* **2025**, *18*, 3574. [CrossRef]
30. Anttila, S.; Döhler, J.S.; Oliveira, J.G.; Boström, C. Grid Forming Inverters: A Review of the State of the Art of Key Elements for Microgrid Operation. *Energies* **2022**, *15*, 5517. [CrossRef]